# Extrusion-based Integrative Chemistry : Generation and applications of inorganic fibers

Natacha Kinadjian, Martin Depardieu, Elisabeth A. Hillard, Rénal Backov

C. R. Chimie 19 (2016) 674–683

Contents lists available at ScienceDirect

Comptes Rendus Chimie

www.sciencedirect.com

Account/Revue

# Extrusion-based *Integrative Chemistry*: Generation and applications of inorganic fibers

## *Chimie intégrative dédiée à l'extrusion : de la synthèse de fibres inorganiques à leurs applications*

Natacha Kinadjian, Martin Depardieu, Elizabeth A. Hillard, Rénal Backov*

*Université de Bordeaux, Centre de Recherche Paul Pascal, office 115, UPR 8641-CNRS, 115 Avenue Albert Schweitzer, 33600 Pessac, France*

ARTICLE INFO

*Article history:*
Received 8 June 2015
Accepted 21 September 2015
Available online 21 February 2016

*Keywords:*
Extrusion
Sol-gel
Hybrid materials
Fibers
Sensors
Photonics
Photocatalysis

ABSTRACT

In this review we depict how fibers can be obtained by combining sol-gel and polymer chemistry with extrusion processes acting as an external shaping mode. Thanks to this *Integrative Chemistry*-based synthetic path, it was possible to organize nano-building blocks such as $V_2O_5$ ribbons and ZnO nanorods on a greater length scale yielding highly anisotropic fibers. It has been demonstrated that when aligning a whole population of nano-building block objects along a single main axis, collective properties were obtained, thereby enhancing their sensing, mechanical or photonic properties. This method can be extended toward fiber morphogenesis by using isotropic nanoparticles such as $TiO_2$, and can be scaled-up toward the one-step generation of several hundred meter long fibers with both high surface to volume ratio and high surface roughness. Specifically, when addressing photocatalytic-based VOC pollutant degradation, these $TiO_2$ fibers appear to be outstanding candidates regarding both pollutant degradation and associated mineralization (production of water and carbon dioxide).



*Mots-clefs:*
Extrusion
Sol-gel
Matériaux hybrides
Fibres
Senseurs
Photonique
Photo-catalyse

RÉSUMÉ

Avec cette mini-revue, nous montrons comment des fibres macroscopiques peuvent être générées en combinant chimie sol-gel et polymères avec le procédé d'extrusion induisant la mise en forme macroscopique. En utilisant cette *chimie intégrative*, il est possible de mettre en forme aux grandes échelles des nano-briques élémentaires comme des rubans de $V_2O_5$, des bâtonnets de ZnO générant des fibres dont les textures et les propriétés sont fortement anisotropes. Nous démontrons qu'en alignant une population de nano-objets de manière unidirectionnelle, les propriétés collectives induites permettent d'obtenir des applications exaltées, que ce soit dans les domaines des sondes sensorielles ou de la photonique. Cette approche peut être étendue *via* la mise en forme aux grandes échelles de nanoparticules isotropes de $TiO_2$, avec de plus une mise en œuvre semi-industrielle en une seule étape permettant à la fois de générer plusieurs centaines de mètres de fibre en continu et de contrôler indépendamment le rapports entre volumes et surfaces spécifiques ainsi que la rugosité de ces fibres. Ainsi, dans le domaine de la photo-catalyse, ces fibres apparaissent comme de remarquables candidats pour la purification de l'air, où ils

* Corresponding author.
*E-mail address:* backov@crpp-bordeaux.cnrs.fr (R. Backov).

http://dx.doi.org/10.1016/j.crci.2015.09.012

excellent à la fois pour la dégradation de polluants volatils et pour leur minéralisation, c'est-à-dire leur transformation en eau et dioxyde de carbone.



## 1. Introduction

In nature, shape and functionality are intimately connected: the allotropic form of a given system is often as important as its composition. When we look at the staggering diversity of proteins, we should keep in mind that the majority of their innumerable biological functions actually rely on a very limited number of atomic elements. From the 19th century [1] until just recently, scientists studying protein composition were unable to explain their inner workings. It was not until biochemists were able to successfully describe tertiary protein structures [2] that we were able to understand that protein shapes were of primary importance for fine-tuning or specializing their intrinsic functionality. Similarly, in natural inorganic architectures, the morphology of silica — used both by diatoms and sponges as a skeleton material — is not simply a question of mechanical robustness. For example, diatoms possess intricate patterns on the surface of their silica shell, or frustul, that help in mass transport of nutrients to their pores [3], while the skeletal elements, or spicules, of sponges can act as optical fiber-like materials [4], guiding light through the sponge core, possibly permitting a symbiotic relationship with green algae [5]. Hence, the same molecular precursor can be given very different properties and functions when shaped differently over several length scales. In this vein, Mann proposed to derive synthetic mechanisms from the observation of such organisms to create bio-inspired materials, grouped under the term "integrative synthesis" [6]. Integrative syntheses refer to the combination of "self-assembled organic templates (transcriptive syntheses), cooperative assemblies of templates and building blocks (synergistic synthesis), and spatially restricted reaction fields (morpho-synthesis)". Sanchez further emphasized that integrative syntheses would be able to create materials with complex morphologies by combining "(i) transcription, using pre-organized or self-assembled molecular or supramolecular moulds of organic (possibly biological) or inorganic nature, used as templates to construct the material by nanocasting and nanolithographic processes; (ii) synergetic assembly, co-assembling molecular precursors and molecular moulds in situ; (iii) morphosynthesis, using chemical transformations in confined geometries (microemulsions, micelles and vesicles) to produce complex structures" [7]. The concept of *Integrative Chemistry* [8] hence emerged as "the integration of the sol-gel process, inorganic chemistry, lyotrope mesophases, supramolecular architectures, air-liquid foams, biliquid foams, external fields, organic polymers, nanofunctionalization and nanotexturation, (…) [, which] offers the possibility of achieving new architectures at various length scales and with enhanced properties." It uses a multidisciplinary toolbox, drawing from several domains of the chemical sciences to create building blocks while connecting or assembling them at different length scales, using different driving forces, structuring mechanisms and reactions to rationally design advanced functional materials. These materials may address multiple dimensionalities, particles [9,10], fibers [11,12], films [13] or monolithic foams [14,15].

This paper will treat *Integrative Chemistry* as applied to sol-gel chemistry when combined exclusively with the extrusion shaping mode to address fiber generation. The goal here is certainly not to be exhaustive, but we will show how, through the specific extrusion-based *Integrative Chemistry* synthetic path, it is possible to tune the nature, texture, shape and topology of fibers, and to correlate these properties with enhanced and targeted applications. Also, we will briefly treat the electrospinning process to introduce extrusion-based fiber morphogenesis.

## 2. Fiber morphogenesis and applications thereof

Fibers are very interesting structures as they are highly anisotropic, and present a high specific surface area due to their high surface/volume ratio. Manufacturing of very long organic fibers is a well-known technique, but the preparation of inorganic/organic composites or pure inorganic fibers is more challenging. In this section, we will focus on extrusion-based methods, although other methodologies can also be employed.

### 2.1. Advantages and drawbacks of electrospun-based fiber morphogenesis

Among the methodologies to create polymer fibers, electrospinning is by far the most popular because of its low cost and simplicity [16]. This method has also been extended to composite formulations, with carbon nanotubes (CNTs) or inorganic nanoparticles, such as $TiO_2$ [17] and ZnO, being added to the polymer solution. The polymer can be removed by thermal treatment afterwards, leading to purely inorganic fibers. The major issues with this technique is that the fibers are randomly oriented and that once the fibers are collected, their structure is fixed as they are difficult to handle (their diameter is in the range of a few nanometers to a few micrometers). Most current reports dealing with inorganic fibers derived from electrospinning deal with electrospun suspensions of premade inorganic particles or precursors, diluted in a polymer solution that provides suitable viscoelastic properties for the electrospinning process. The polymer acts as a support and is removed afterwards by calcination to yield the fully inorganic 1D object. This approach has been very successful for many systems [18,19], but it suffers from a very low atom economy. Indeed, the polymer content of the as-obtained fibers is often 95 wt% or more, so that most of the initial matter is destroyed after calcination. Besides cost

and safety issues, this method often results in a collapse of the material upon calcination, so porosity, particle size, etc. are not preserved. To overcome this problem, Maneeratana and Sigmund proposed "direct hybrid electrospinning" a few years ago [20]. The method is based on the electrospinning of a sol-gel solution containing inorganic molecular precursors, most often alkoxides, and organic oligomers. Contrary to regular electrospinning and because the metal alkoxides act as cross-linkers between the organic component, short oligomers in low concentration are sufficient to provide enough viscosity for electrospinning. As a result, an organic content as low as 25 wt% can be obtained.

### 2.2. Extrusion-based fiber morphogenesis

There are two different ways to extrude polyvinyl alcohol (PVA) based composite fibers. The first is a process that was introduced by Vigolo *et al.* in 2000 [21] for PVA/CNT fibers. This process consists of linking the nanoparticles together in a rotating bath containing the PVA solution. For this purpose, the surface of the CNTs is first functionalized using amphiphilic molecules in order to disperse them in an aqueous solution. When the CNTs are introduced to the rotating bath beaker, the PVA chains are adsorbed onto their surface and act as a bridge between them, the PVA chains being connected to each other by hydrogen bonds. This principle was later adapted for the extrusion of vanadium oxide ($V_2O_5$)/PVA composite fibers [22]. The major drawbacks of this technique are: (i) it can only be applied to nanoparticles with a very high aspect ratio, and (ii) the weight percentage of nanoparticles inside the fibers is generally low. For particles that are either isotropic or anisotropic but with a moderate aspect ratio, another method involving polymer dehydration using a salt solution was favored. This method was first described by Sakurada *et al.* in 1985 [23]. It was also adapted to the extrusion of PVA/CNT fibers [24], by extruding a PVA/CNT sol into a concentrated solution of sodium sulfate ($Na_2SO_4$). The flocculation of the PVA chains results from the interaction between the $Na^+$ ions and the water molecules in the PVA chains, leading to a local dehydration of the PVA/CNT fibers. The problem with this dehydration technique is that salt residues remain inside the fibers and thus washing of the fibers after formation is required.

#### 2.2.1. $V_2O_5$ fibers as alcohol sensors

*2.2.1.1. Effects of applied shearing rates on the sensing and mechanical properties of the fibers.* The shearing rate, $\gamma$, associated with the extrusion process, is strongly related to the needle position within the rotating beaker. In this study, we modified the needle position in order to estimate the effect of shearing rate on the alignment of the ribbon sub-units within the macroscopic fiber, as well as on the specific properties of the fiber. During all extrusion processes, the needle was maintained horizontal and tangentially to the beaker rotation, at the same depth (around 1 cm), while keeping the beaker rotating speed constant. Three needle positions were evaluated, and it was found that the shearing rate rose as extrusion proceeded towards the edge of the beaker. Considering the PVA solution linear speed ($V_b$, associated with the different needle positions), the vanadium oxide sol extrusion speed ($V_e$) and the needle diameter ($d = 400$ μm), we can estimate the shear rate ($\gamma$) associated with each position using Eq. (1) [25]:

$$\gamma = \frac{dV}{dx} \approx \frac{(V_b - V_e)}{(d/2)} \quad (1)$$

Thus the three different needle positions, ranging from the center to the edge of the beaker, correspond to $\gamma = -158\ s^{-1}$, $100\ s^{-1}$ and $235\ s^{-1}$, respectively. The negative shear strength, associated with the needle position at the center, indicates that the speed of the vanadium oxide flow is higher than that of the rotating beaker. In this case, the size of the vanadium oxide extruded flow should increase when compared to the two other applied shear strengths, thus leading to larger fiber diameters. By varying the shear rate imposed during the extrusion process it is possible to tune the fiber's macroscopic morphology (Fig. 1a–f) as well as the preferential alignment of the ribbon sub-units (Fig. 1g,h,j, where we see that the fiber birefringence increases with the strength of the applied shear rate).

It is also possible to estimate the average tilt angle of the nano-ribbons toward the macroscopic fiber's main axis, providing more quantitative results. To this end, we performed small angle X-Ray scattering (SAXS) experiments. A representative SAXS pattern shows an anisotropic diffuse spot around the beam trap [22] corresponding to the main tilt angles of the ribbon, which vary from 17° to 28° as the applied shear rate decreases. As previously observed [22], the scattered intensity, I, of this diffuse spot regularly decreases with the scattering vector modulus $q$ as $q^{-2}$ [26], which corresponds to the form factor of plate-like ribbons. The fiber's mechanical properties should be strongly related to the specific alignment of the nanoscopic ribbon sub-units. For each employed shear rate, several measurements were carried out in order to calculate average mechanical characteristics of each kind of fiber (Fig. 2a). As observed in Fig. 2a, the fibers possess a weak plastic behavior before they break; this plastic regime decreases as the shear rate increases. Given that an increase of the shear rate is associated with a better alignment of the nano-ribbon sub-units parallel to the main fiber axis, this feature is expected. When considering the Young's modulus ($E$), there is a strong enhancement with increasing shear rates, varying from 13 Gpa for the lower shear rate to 22 Gpa for the higher one.

Here again, as the nano-ribbon sub-units are more aligned due to increasing shear rate, both the Young's modulus and rigidity ($\tau$) increase. It should also be mentioned that the Young modulus of these vanadium oxide fibers appear to be in the same range as the best ones obtained for fibers made of carbon nanotubes [25]. In Fig. 2b, we observe that the sensitivity is enhanced (lower detection times) when the fibers are generated using a higher shear rate. However, ribbon alignment and textural mesoporosity, two parameters which should play a crucial role in sensing, are antagonists, i.e. with increasing ribbon

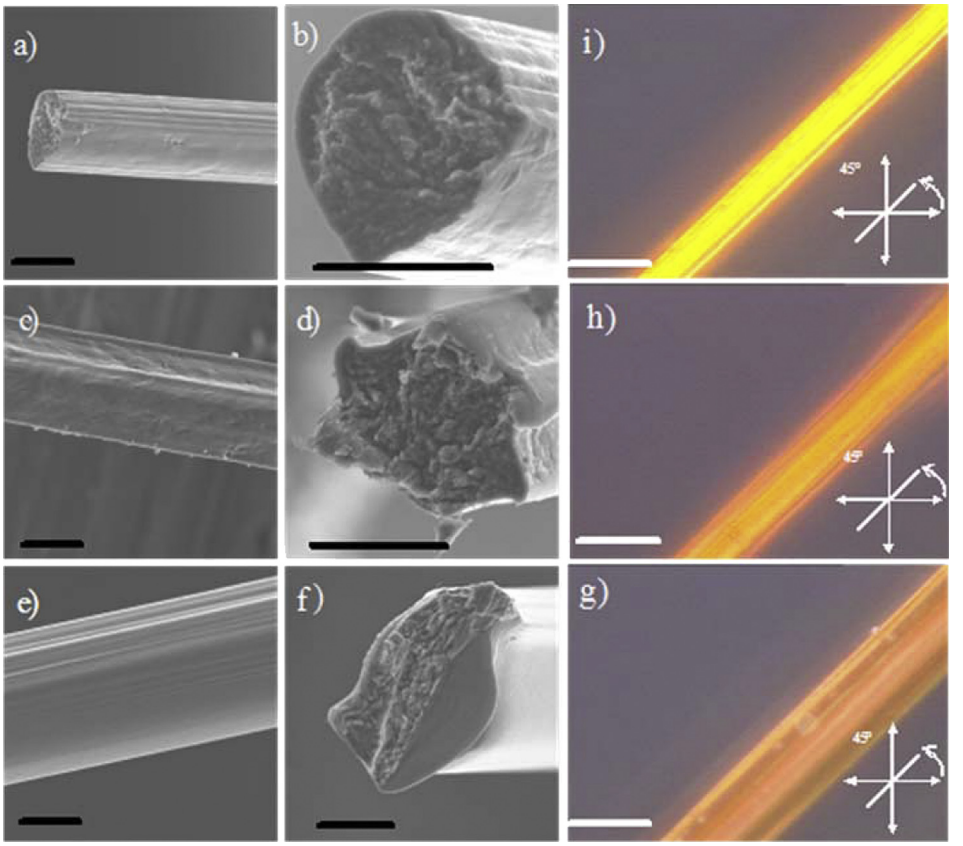


**Fig. 1.** SEM observations on vanadium oxide fibers. Fibers synthesized with $\gamma = 235\ s^{-1}$ (a and b), $\gamma = 100\ s^{-1}$ (c and d) and $\gamma = -158\ s^{-1}$ (e and f). The scale bars represent 20 μm. Vanadium oxide fibers observed through a cross-polarized microscope at 45° between the analyzer and polarizer. Fibers synthesized with $\gamma = 235\ s^{-1}$ (i), $\gamma = 100\ s^{-1}$ (h), and $\gamma = -158\ s^{-1}$ (g). The scale bars represent 50 μm.

alignment, or stacking, the textural porosity should decrease. If we consider that, regardless of shear rate, the final fibers are, at most, poorly mesoporous [25]; the main factor that explains the sensitivity variation with the applied shear rate is therefore ribbon alignment. Thus we can state that the better alignment of the nano-ribbons, obtained through a higher shear rate, favors the electron depletion phenomenon and thus fiber sensitivity [19]. On the other hand, as porosity is limited, once the external surface of the vanadium oxide has been reduced through alcohol oxidation, conductivity starts to decrease as the native $V^{4+}$ species act as a hole potential for the electrons, minimizing thereby the conductivity.

We have demonstrated that the nanoscopic ribbon subunit alignment, tuned *via* the shear rate applied during the extrusion process, appears to be a good tool to adjust the final mechanical and sensing properties of the as-synthesized fibers. However, the thermodynamic stability during sensing was lacking. Therefore, the next study was dedicated to increasing fiber mesoporosity, using sacrificial latex nanoparticles, as well as promoting vanadium oxide crystallization through a thermal treatment. We thereby wished to determine if the specific alignment of the ribbons, the associated mesoporosity and the $V_2O_5$ crystallinity are involved, either in a cooperative or partitioning fashion, in tuning the final fiber sensitivity [27].

*2.2.1.2. Effects of combining applied shear rates and latex inclusion content on the fiber's sensing and mechanical properties.* Composite vanadium oxide/PVA/latex fibers have been generated by using an extrusion process (Fig. 3a–g) [27]. Specifically, inorganic vanadium oxide fibers enable the detection of 0.1 ppm of ethanol within 3–5 s at 42 °C, which is one of the highest sensitivities to date concerning alcohol sensors (Fig. 3h–i).

More importantly, by varying the starting latex inclusion content (10, 30, and 60 wt%), the shear rates associated with the gel extrusion process, and the presence or absence of a thermal treatment, we were able to segregate each parameter involved in the sensing properties of the fibers, i.e., the organic concentration, the degree of vanadium oxide ribbon alignment, and the induced porosity reached upon latex removal. The sensitivity was strongly enhanced by the removal of the insulators PVA and latex by the applied thermal treatment, but was not dependent on the porosity. While varying porosity did not induce much fluctuation in detection times, the thermodynamic stability was strongly improved with increased porosity. On the other hand, we noticed that the higher porosity is not of primary importance toward the sensing-cycling properties of the final porous vanadium oxide fibers. Overall, the conclusion was that the parameters involved in the sensing properties were not acting in a cooperative fashion but

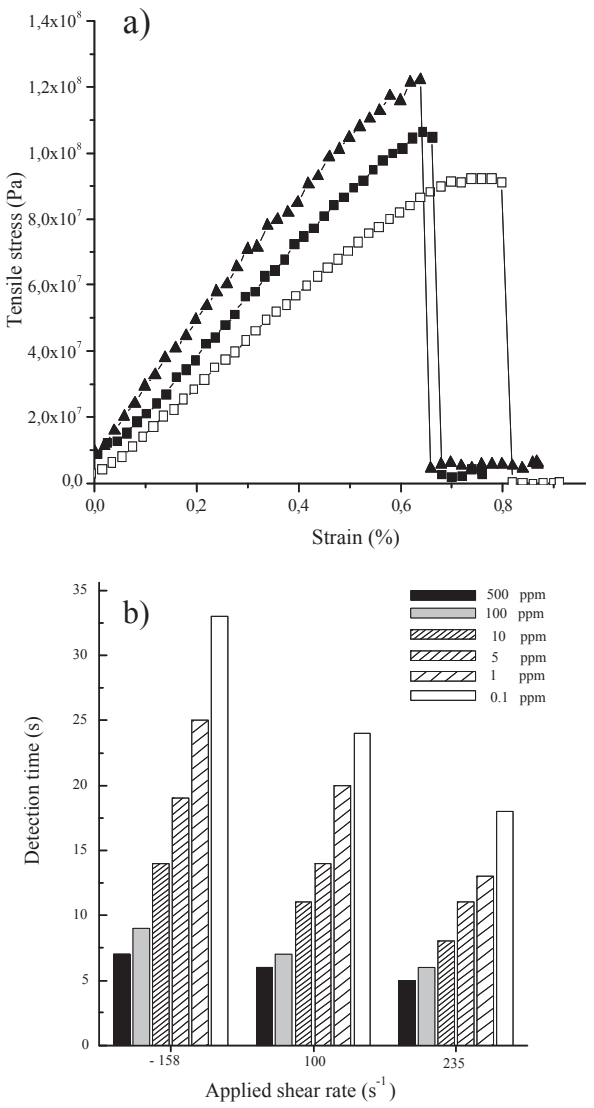


**Fig. 2.** a) Mechanical properties of vanadium oxide fibers for each shearing rate. Measurements were performed at a strain rate of 0.3 mm/min. □ $\gamma = -158\ s^{-1}$, ■ $\gamma = 100\ s^{-1}$ and c) ▲$\gamma = 235\ s^{-1}$ .b) Histogram depicting ethanol sensitivities of vanadium oxide fibers at 40 °C. The experimental set-up is placed above a beaker containing ethanol with concentrations of 500–0.1 ppm. Ethanol has been diluted with THF because THF does not promote the effect over the conductivity cell. The provided results have been obtained for a single vanadium oxide fiber.

rather in a strong partitioning one. For instance, if we increase the fiber sensitivity with the removal of PVA and latex, we will increase the fiber thermodynamic stability on one hand, but on the other hand, the fiber cycling properties will be strongly diminished.

### *2.2.2. Composite fibers prepared by polymer dehydration/reticulation*

*2.2.2.1. ZnO macroscopic fibers for photonic applications.* We then turned our attention to macroscopic fibers that contain ZnO nanorods for photoluminescence applications [28]. Measurements on a single nanorod are difficult but being able to align a whole population of ZnO nanorods along a single axis could allow us to evaluate the macroscopic effect of collective alignment. Moreover, we aimed to verify if the alignment of a population of ZnO nanorods within the fiber would create a synergetic response to produce anisotropic photoluminescence behavior. As ZnO possesses a much lower aspect ratio than CNTs or $V_2O_5$ ribbons, it was necessary to use the dehydration method during the extrusion process [28]. The initial extrusion shear rate was chosen according to that required for maximum alignment of the $V_2O_5$ ribbons inside the fibers [25].

The alignment of the ZnO particles was improved by a post-synthesis stretching of the hybrid fibers above the PVA glass transition at T = 85 °C. An evolution of the mean orientation angle of the nanorods compared to the fiber main axis depending on the elongation percentage is presented in Fig. 4e. Fig. 5a displays the photoluminescence (PL) spectra obtained for the non-stretched fibers with the laser oriented at 90° or 0° with respect to the main axis. Their photoluminescence was compared with that of ZnO particles alone. The PL spectrum of ZnO particles showed an intense near band edge emission with no green emission, which confirmed that the ZnO particles were highly crystalline with no structural defects [29–32].

For non-stretched fibers, a similar response was observed for both the longitudinal and transversal measurements (isotropic response). In contrast (Fig. 5b), the stretched fibers displayed huge differences: the intense UV emission detected when the laser beam was oriented perpendicular to the fiber main axis (90°) was almost suppressed when the laser beam was oriented parallel (0°). This difference can result only from the alignment of ZnO nanorods within the composite fiber, and their resulting orientation with the incident beam. If the propagation vector $\vec{k}$ of the incident light is normal to the fiber and concomitantly to the aligned ZnO nanorods' main axis, then the light wave, polarized with its electric field $\vec{E}$ (perpendicular to $\vec{k}$) parallel to the axis of the fiber will give an optimal interaction with the absorption transition dipole of ZnO ($\vec{\mu}_{ZnO}$), and $\vec{E} \cdot \vec{\mu}_{ZnO}$ will be maximized. If the propagation vector $\vec{k}$ of the incident light is parallel to the main axis of the fiber, then $\vec{E} \cdot \vec{\mu}_{ZnO}$ is almost equal to zero, and almost no PL will be detected [33,34].

*2.2.2.2. $TiO_2$ macroscopic fibers dedicated to photocatalysis for air purification.* A number of recent studies have reported the fabrication of one-dimensional $TiO_2$ for photocatalysis applications [16,35,36]. Indeed, the large surface-to-volume ratio, the enhanced adsorption of various reactants, and the favorable morphology for prolonging reactant-catalyst contact were expected to improve the properties of these materials [37]. Recently, we decided to generate such structures *via* the extrusion process using a salted solution to induce polymer flocculation [38]. Surfactant molecules were used in the nanoparticle synthesis in order to make the fiber mesoporous. Therefore, three types of titanium nanoparticles (nanorods and spheres) were synthesized, extruded as nanocomposite fibers, and

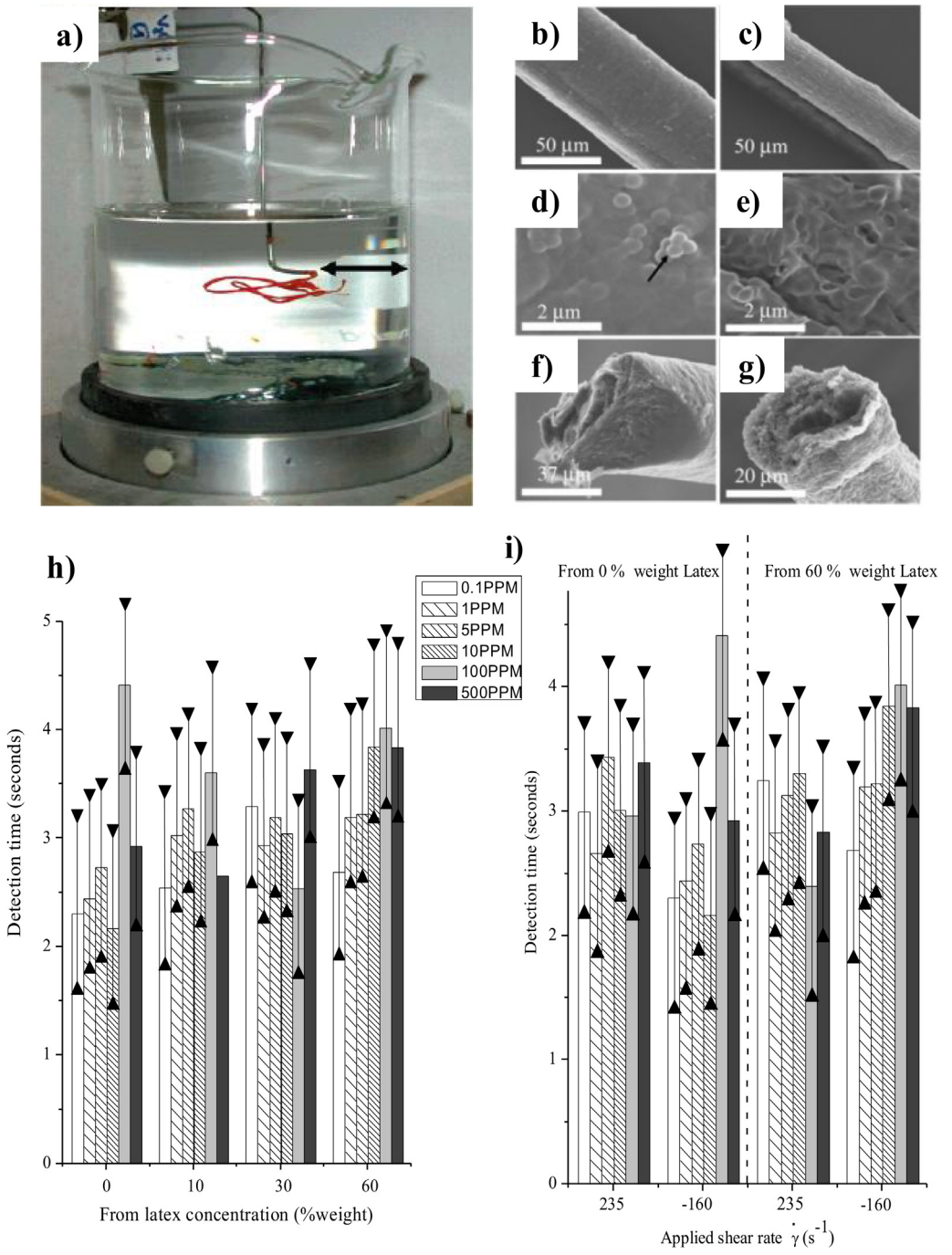


**Fig. 3.** a) Extrusion system of $V_2O_5$/PVA composite fibers. Histograms depicting the ethanol sensitivities at 42 °C for calcined fibers. SEM pictures of fibers obtained with a 60 wt% latex concentration and at a shear rate of −158 $s^{-1}$ (b,d, and f) without thermal treatment and (c, e, and g) after thermal treatment at 350 °C. The black arrow indicates an aggregate of the latex nanoparticles. The experimental setup has a fiber placed above a beaker containing ethanol for which the concentration varies from 500 ppm down to 0.1 ppm. (h) Effect of latex contents at 235 $s^{-1}$ and (i) effects of latex contents and applied shear rate [27].

processed in order to evaluate how the fiber properties influence photocatalytic degradation and mineralization of acetone.

Upon calcination at 450 °C in air, stable macroscopic fibers containing anatase nanoparticles were generated. The thermal treatment created some mesoporosity by burning away the original PVA matrix and residual surfactant molecules trapped in the $TiO_2$ structure (Fig. 6a–d).

Photocatalytic efficiency of the $TiO_2$ fibers at the gas-solid interface demonstrated a lower degradation rate, but a higher mineralization percentage, than that of the

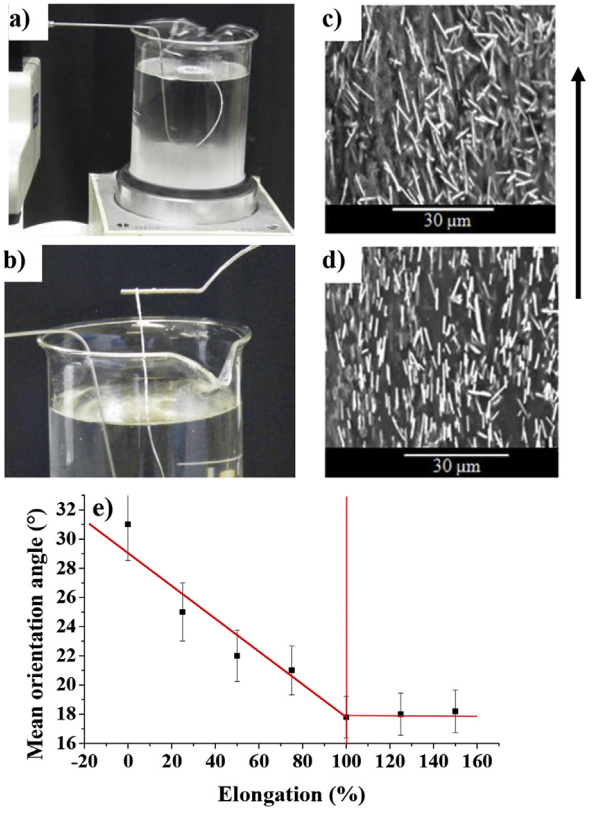


**Fig. 4.** a) Typical extrusion where the PVA/ZnO hybrid sol is injected through a syringe needle into a rotating beaker containing a $Na_2SO_4$ saturated water solution, b) as-synthesized hybrid fibers extracted by hand from the beaker. SEM images of c) a non-elongated fibers and d) of a 150%-elongated fiber. The black arrow indicates the fibers' main axis. Figure e) presents the mean orientation angle of the ZnO nanorods compared to the fibers' main axis as a function of the stretching percentage [28].

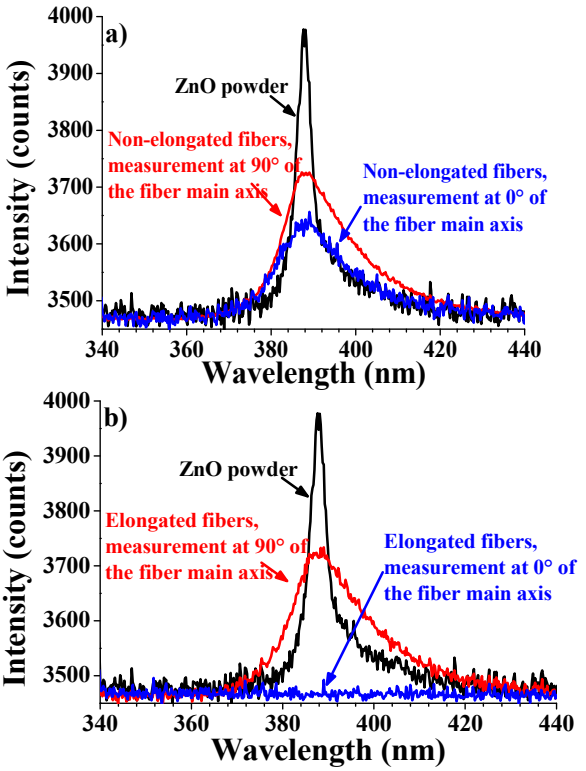


**Fig. 5.** PL spectra of a) non-stretched and b) stretched ZnO fibers measured upon the excitation beam oriented at 90° (in red, perpendicular to the fiber main axis) and 0° (in blue, parallel to the fiber main axis). The black curve corresponds to the PL spectrum of pure ZnO nanorods (reference) [28].

commercial Quartzel® fibers (Fig. 6e). It was obvious that the overall size of our materials will not allow them to compete – at this stage – with optimized commercial catalysts. This study allowed us nonetheless to understand the influence of structural factors on tailor-made materials, which will be used in the future to optimize their photocatalytic efficiency. For example, we demonstrated that surface roughness has an impact on acetone degradation, and that increasing this surface roughness could help in increasing photocatalytic performance. On the other hand, we observed that the surfactant nature (linked to the specific surface area) did not impact the photocatalytic performance, as particles synthesized with Tergitol NP-10 gave equivalent results to those synthesized with TTAB. Unfortunately, we could not draw clear conclusions on the influence of the nanoparticle shape on photocatalytic performance.

Also, we have identified two main shortcomings that need to be addressed to optimize the as-synthesized fiber photocatalytic properties. First, it will be important to minimize the amount of carbon and salt content while maintaining the anatase phase during the thermal treatment. The second main issue is to optimize the light access into the fiber core by reducing the fiber's diameter. Indeed, we have demonstrated that reducing the fiber's diameter by crushing them into powder, significantly improving their efficiency.

*2.2.2.3. $TiO_2$ macroscopic fibers dedicated to photocatalysis: semi-industrial process.* In this study, we made use of a continuous industrially scalable extrusion process employing hybrid sols of amorphous titania nanoparticles, PVA and optional latex nanoparticles. This process allowed the continuous generation of hybrid $TiO_2$/latex/PVA or $TiO_2$/PVA macroscopic fibers. Upon thermal treatment in air, we obtained biphasic porous fibers containing the anatase phase of $TiO_2$ with 10–15% brookite. These fibers were several hundred meters in length and provided significantly improved phototocatalytic efficiency compared to the previous work mentioned above [39].

Considering the scalable linear fiber wet-spinning process in use (Fig. 7), several hundred meters of these processed hybrid fibers could be obtained continuously. Once calcined, the fiber morphology and topology were studied through SEM investigations (Fig. 1b–g). Overall, the fibers present a flattened shape with a width ranging from 40 to 47 µm and a thickness ranging from 10 to 17 µm.

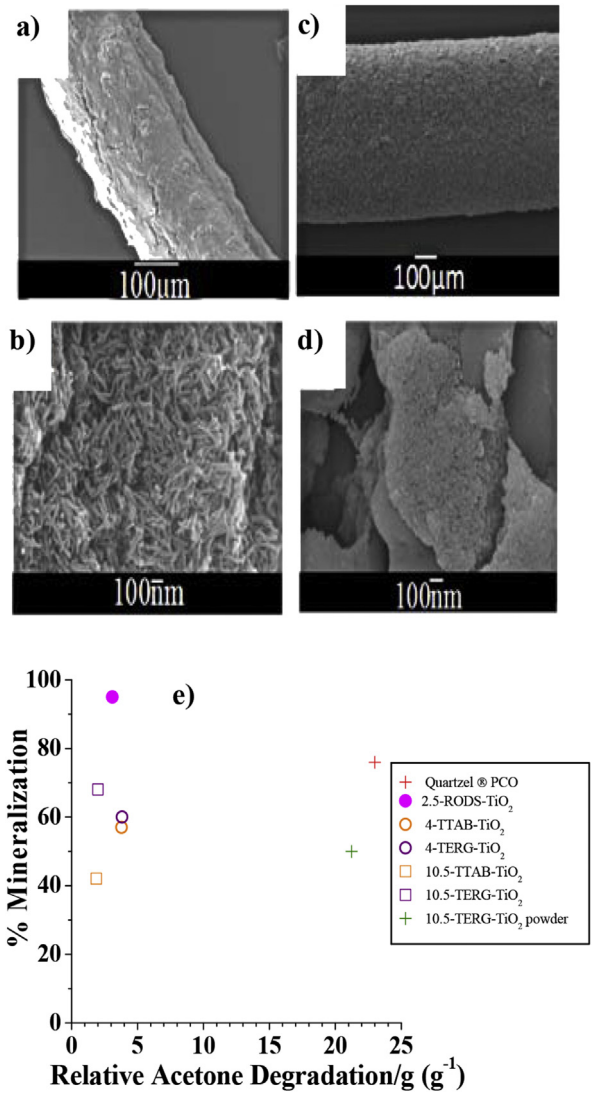


**Fig. 6.** SEM images of the different thermally treated $TiO_2$ fibers: 2.5-RODS-$TiO_2$ fiber a) and b), 10.5-TERG-$TiO_2$ fiber c) and d). e) Comparison between the final acetone degradation percentage and the final mineralization percentage of the five types of fibers, the powdered 10.5-TERG-$TiO_2$ fibers, and the Quartzel® under irradiation of acetone at 366 nm (RH 15%, temperature 22 ± 2 °C, initial acetone concentration 45 ppmv, air flow rate 3.3 L $min^{-1}$) [38].

Typical curves of acetone concentration against time were compared (Fig. 8a), and from the fit of the pseudo first order kinetics, the reaction rate constants *k*, normalized per gram of media, were determined (Fig. 8b).

Encouragingly, the efficiency of these new fibers ($k = 0.11$ $min^{-1}$ $g^{-1}$ on average) is three times higher than that of the 1.0 processed fibers ($k = 0.037$ $min^{-1}$ $g^{-1}$ on average) under strictly identical conditions [39,40]. More importantly, the new fibers present rate constants of the same order of magnitude as the commercial Quartzel®PCO, which might make them competitive from a commercial point of view. In our previous studies [38,40], it was shown that, under our experimental conditions, the photocatalytic performance of the fibers was not primarily affected by their specific surface area, but rather by their mesoscopic roughness, diameter size, and macroscopic surface topology. The mineralization percentage was calculated to be between 200 and 400 min of irradiation and was found to be stable in this range (Fig. 8c). The mineralization percentage varied from 51% ($TiO_2$-latex-indus) to 72% (Quatzel PCO), with no significant difference between the $TiO_2$-latex-indus and $TiO_2$-indus fibers (51% and 55%, respectively). From this result, we can deduce that despite the high acetone degradation rate, the topology of the new fibers was not yet fully optimized for acetone degradation. However, it has to be noted that no other gaseous by-products issued from acetone degradation were detected in the gas phase. This means that any possible intermediate oxidation products probably remained strongly adsorbed on the photocatalytic fibers.

By comparing the $TiO_2$-indus fibers with the $TiO_2$-latex-indus fibers, we also conclude that latex beads, used as sacrificial templates, did not improve the photocatalytic performance (Fig. 8). On the contrary, $TiO_2$-latex-indus fibers are slightly less efficient than those of $TiO_2$-indus. As their diameters are on the same order of magnitude, this difference in reaction kinetics can be attributed to a difference in the surface topology. Indeed, as described earlier, latex particles prevent PVA chain alignment, which caused a misalignment of the fiber striation. In this case, we hypothesized that the air-flux is disturbed through hydrodynamic turbulences minimizing thereby the gas-solid contact time when compared with the $TiO_2$-indus fibers with a well-aligned striation along the fiber main axis (not shown here). Indeed, the use of a new flow-through recirculating reactor loop with variable LED irradiation at 365 nm yielded fibers showing the same efficiency for acetone and heptane degradation, while offering better activity for toluene degradation and mineralization when compared with the Quatzel PCO commercial product [41].

## 3. Conclusions

The shape of materials is of primary importance when considering their properties; the best performance being generally obtained with complex structures. Such structures can be generated by using the *Integrative Chemistry* concept, which is an interdisciplinary synthetic path where, in this paper, the tools of sol-gel, inorganic, and polymer chemistry are combined with external shaping modes such as lyotropic mesophases, foams, and extrusion [8]. Recently, one-dimensional structures such as fibers have been obtained by combining sol-gel and polymer chemistry with extrusion processes [25,27,28,38–42]. Thanks to this method, it was possible to organize nano-building blocks such as $V_2O_5$ ribbons and ZnO nanorods in highly anisotropic materials. It has been demonstrated that by aligning a whole population of nano-building blocks along a single main axis, it was possible to promote collective properties, and by doing


**Fig. 7.** Overall unidirectional extrusion process. a) Syringe pump used for the injection of the starting solution in the coagulation bath, b) coagulation bath saturated salt solution of $Na_2SO_4$ at 320 g $L^{-1}$, the injection of the solution into the bath; the black arrow indicates the fiber position, c) the exit of the solid fiber from the bath; the black arrow indicates the fiber position, d) fiber passing through the washing bath (aqueous solution containing sodium tetraborate at 0.1 mol $L^{-1}$); the white arrow indicates the $TiO_2$ fiber being extracted continuously from the wash bath, e) drying of the fibers using infrared lamps with a roller conveyor belt coated with Teflon; the white arrow indicates the fiber, f) fiber winding [39].

so, to enhance sensing, mechanical, and optical properties. Also, this method can be applied for the generation of fibers containing isotropic species such as $TiO_2$ nanoparticles, and can be scaled up for the generation of hundred meter long fibers with high surface to volume ratio and high surface roughness. Thanks to their specific features, these fibers interact in an optimized way with their environment and are as efficient as commercial products used for air depollution. From these examples, we can imagine that the next step will be to combine fibers with nano-building blocks bearing different properties to create multifunctional and multiresponsive materials.

Overall, we have shown here how chemistry, physical chemistry and process chemistry are advantageously coupled to generate advanced functional fibers. Furthermore, we have emphasized how nano-building block flocculation can be induced and controlled in the jetting mode of extruded fluids. This feature is just another example of how integrative chemistry allows positioning chemical

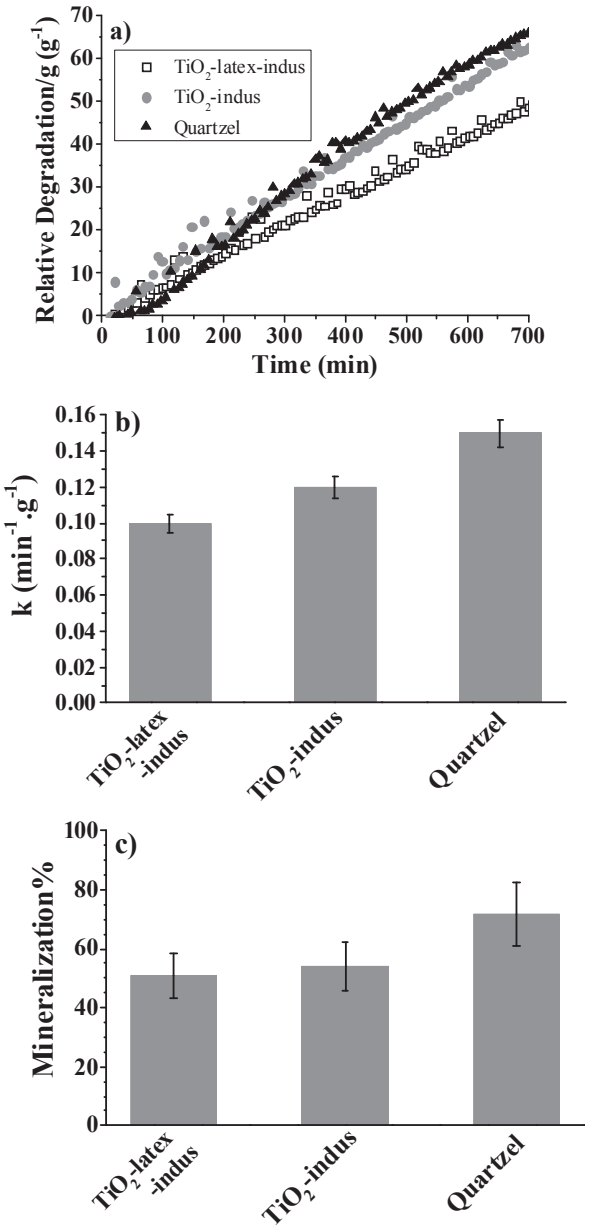


**Fig. 8.** Results for the photocatalytic properties of the fibers: a) % acetone degradation/g of media against time; b) pseudo-first-order rate constants of acetone degradation calculated from the degradation rate by gram of media; c) % mineralization between 200 and 400 min under irradiation of gaseous acetone at 366 nm (RH 15%, temperature 22 ± 2 °C, initial acetone concentration 50 ppmV, air flow rate 3.3 L $min^{-1}$) [39].

reactors within the geometric space, specificity from which rational design of advanced functional materials can be reached with ease [43].

## References

[1] G.J. Mulder, J. Für Prakt. Chem. 16 (1839) 129.
[2] H. Muirhead, M.F. Perutz, Nature 199 (1963) 633.
[3] M.S. Hale, J.G. Mitchell, Aquat. Microb. Ecol. 24 (2001) 287.
[4] V.C. Sundar, A.D. Yablon, J.L. Grazul, M. Ilan, J. Aizenberg, Nature 424 (2003) 899.
[5] E. Gaino, M. Sara, Mar. Ecol. Prog. Ser. 108 (1994) 147.
[6] S. Mann, S.L. Burkett, S.A. Davis, C.E. Fowler, N.H. Mendelson, S.D. Sims, D. Walsh, N.T. Whilton, Chem. Mater. 9 (1997) 2300.
[7] G.J.D.A.A. Soler-Illia, C. Sanchez, B. Lebeau, J. Patarin, Chem. Rev. 102 (2002) 4093.
[8] R. Backov, Soft Matter 2 (2006) 452.
[9] M. Nollet, M. Depardieu, M. Destribats, R. Backov, V. Schmitt, Part. Part. Syst. Charact. 30 (2013) 62.
[10] M. Depardieu, M. Nollet, M. Destribats, V. Schmitt, R. Backov, Part. Part. Syst. Charact. 30 (2013) 185.
[11] L. Biette, F. Carn, M. Maugey, M.F. Achard, J. Maquet, N. Steunou, J. Livage, H. Serier, R. Backov, Adv. Mater. 17 (2005) 2970.
[12] N. Kinadjian, M.F. Achard, B. Julián-Lõpez, M. Maugey, P. Poulin, E. Prouzet, R. Backov, Adv. Funct. Mater. 22 (2012) 3994.
[13] C.M. Leroy, C. Olivier, T. Toupance, M. Abbas, L. Hirsch, S. Ravaine, R. Backov, Solid State Sci. 28 (2014) 81.
[14] F. Carn, A. Colin, M.F. Achard, H. Deleuze, Z. Saadi, R. Backov, Adv. Mater. 16 (2004) 140.
[15] M. Destribats, B. Faure, M. Birot, O. Babot, V. Schmitt, R. Backov, Adv. Funct. Mater. 22 (2012) 2642.
[16] D. Li, Y. Xia, Adv. Mater. 16 (2004) 1151.
[17] S. Mo, W. Ching, Phys. Rev. B: Condens. Matter 51 (1995) 13023.
[18] R. Ramaseshan, S. Sundarrajan, R. Jose, S. Ramakrishna, J. Appl. Phys. 102 (2007) 111101.
[19] W. Sigmund, J. Yuh, H. Park, V. Maneeratana, G. Pyrgiotakis, A. Daga, J. Taylor, J.C. Nino, J. Am. Ceram. Soc. 89 (2006) 395.
[20] V. Maneeratana, W.M. Sigmund, Chem. Eng. J. 137 (2008) 137.
[21] B. Vigolo, A. Pénicaud, C. Coulon, C. Sauder, R. Pailler, C. Journet, P. Bernier, P. Poulin, Science 290 (2000) 1331.
[22] L. Biette, F. Carn, M. Maugey, M.-F. Achard, J. Maquet, N. Steunou, J. Livage, H. Serier, R. Backov, Adv. Mater. 17 (2005) 2970.
[23] I. Sakurada, Polyvinyl Alcohol Fibres, M. Dekker, New York, 1985.
[24] C. Mercader, V. Denis-Lutard, S. Jestin, M. Maugey, A. Derre, P. Poulin, J. Appl. Polym. Sci. 125 (2012) 191.
[25] H. Serier, M.F. Achard, O. Babot, N. Steunou, J. Maquet, J. Livage, C.M. Leroy, R. Backov, Adv. Funct. Mater. 16 (2006) 1745.
[26] J. Livage, O. Pelletier, P. Davidson, J. Sol-gel Sci. Technol. 19 (2000) 275.
[27] C.M. Leroy, M.-F. Achard, O. Babot, N. Steunou, P. Masse, J. Livage, L. Binet, N. Brun, R. Backov, Chem. Mater. 19 (2007) 3988.
[28] N. Kinadjian, M.-F. Achard, B. Julián-lópez, M. Maugey, P. Poulin, E. Prouzet, R. Backov, Adv. Funct. Mater. 22 (2012) 3994.
[29] C.-T. Chien, M.-C. Wu, C.-W. Chen, H.-H. Yang, J.-J. Wu, W.-F. Su, C.-S. Lin, Y.-F. Chen, Appl. Phys. Lett. 92 (2008) 223102.
[30] C. Li, G. Hong, P. Wang, D. Yu, L. Qi, Chem. Mater. 21 (2009) 891.
[31] X. Wang, K. Huo, F. Zhang, Z. Hu, P.K. Chu, H. Tao, Q. Wu, Y. Hu, J. Zhu, J. Phys. Chem. C 113 (2009) 170.
[32] F. Decremps, J. Pellicer-Porres, A. Saitta, J.-C. Chervin, A. Polian, Phys. Rev. B 65 (2002) 092101.
[33] S. Chawla, N. Karar, H. Chander, Phys. B Condens. Matter 405 (2010) 198.
[34] S. Baskoutas, G. Bester, J. Phys. Chem. A 115 (2011) 15862.
[35] S. Madhugiri, B. Sun, P.G. Smirniotis, J.P. Ferraris, K.J. Balkus, Microporous Mesoporous Mater. 69 (2004) 77.
[36] W. Nuansing, S. Ninmuang, W. Jarernboon, S. Maensiri, S. Seraphin, Mater. Sci. Eng., B 131 (2006) 147.
[37] Z. Liu, D.D. Sun, P. Guo, J.O. Leckie, Nano. Lett. 7 (2007) 1081.
[38] N. Kinadjian, M. Le Bechec, T. Pigot, F. Dufour, O. Durupthy, A. Bentaleb, E. Prouzet, S. Lacombe, R. Backov, Eur. J. Inorg. Chem. (2012) 5350.
[39] N. Kinadjian, M. Le Bechec, C. Henrist, E. Prouzet, P. Poulin, W. Neri, S. Lacombe, R. Backov, Adv. Eng. Mater. 17 (2015) 36.
[40] N. Kinadjian, M. Le Bechec, C. Henrist, E. Prouzet, S. Lacombe, R. Backov, ACS Appl. Mater. Interfaces 6 (2014) 11211.
[41] M. Le Bechec, N. Kinadjian, D. Ollis, R. Backov, S. Lacombe, Appl. Catal. B: Environ. 179 (2015) 78.
[42] J. Dexmer, C.M. Leroy, L. Binet, V. Heresanu, P. Launois, N. Steunou, C. Coulon, J. Maquet, N. Brun, J. Livage, R. Backov, Chem. Mater. 20 (2008) 5541.
[43] M. Depardieu, M. Nollet, V. Schmitt, R. Backov, C. R. Chimie 19 (2016) 216–230.